Noble gas systematics in new popping rocks from the Mid-Atlantic Ridge (14 °N): evidence for small-scale upper mantle heterogeneities

Sandrine Péron, Manuel Moreira, Mark D. Kurz, Joshua Curtice, Jerzy S. Blusztajn, Benita Putlitz, V. Dorsey Wanless, Meghan R Jones, Samuel Adam Soule, Eric Mittelstaedt

Title: Noble gas systematics in new popping rocks from the Mid-Atlantic Ridge (14 °N): evidence for small-scale upper mantle heterogeneities

Authors: Sandrine Péron[a*], Manuel A. Moreira[a], Mark D. Kurz[b], Joshua Curtice[b], Jerzy S. Blusztajn[c], Benita Putlitz[d], V. Dorsey Wanless[e], Meghan R. Jones[f], S. Adam Soule[c], Eric Mittelstaedt[g]

Affiliations:

[a] Institut de Physique du Globe de Paris - Sorbonne Paris Cité, UMR CNRS 7154, Université Paris Diderot. 1 Rue Jussieu, 75005, Paris, France

[b] Marine Chemistry and Geochemistry, MS #25, Clark 421, Woods Hole Oceanographic Institution, Woods Hole, MA 02543, United States

[c] Department of Geology and Geophysics, Woods Hole Oceanographic Institution, 02543, Woods Hole, MA, USA

[d] Institute of Earth Sciences, University of Lausanne, Géopolis Building, CH-1015 Lausanne, Switzerland

[e] Department of Geosciences, Boise State University, 83725, Boise, ID, USA

[f] Massachusetts Institute of Technology/Woods Hole Oceanographic Institution Joint Program in Oceanography, 02543, Woods Hole, MA, USA

[g] Department of Geological Sciences, University of Idaho, 83844, Moscow, ID

Corresponding author: Sandrine Péron, peron@ipgp.fr

Abstract: The origin and evolution of terrestrial volatiles is a fundamental question in Earth and planetary sciences. To better address this, it is necessary to estimate the present-day isotopic and elemental composition of volatiles in the mantle, which is difficult because degassing during magma transport to the surface changes the initial elemental composition. However, some basalts are considered to be relatively un-degassed and therefore can be used to determine the concentrations of C, N, H_2O and noble gases in the mantle. This is the case of the so-called popping rock sample 2πD43, found near 14 °N on the Mid-Atlantic Ridge in 1985, which has been considered as a reference for upper mantle isotopic and elemental volatile compositions due to its high gas content. Such gas-rich samples have been recovered in only a few places on mid-ocean ridges but are crucial to characterizing the heterogeneities in mantle composition and therefore the cycling of volatiles on Earth. In order to better understand the occurrence of popping rocks, mantle heterogeneities and volatile cycling on Earth, cruise AT33-03 on *R/V Atlantis* was conducted in 2016 on the Mid-Atlantic Ridge near 14 °N. Popping rocks were found in the same area as sample 2πD43, using the submersible *Alvin*, and their noble gas compositions were determined by step-crushing and laser ablation. A new anaerobic sampling protocol was tested in an attempt to minimize atmospheric contamination, which is ubiquitous in basaltic glass samples used for noble gas analyses, and to evaluate laser extraction techniques. Preliminary step-crushing results suggest that the new anaerobic sampling protocol reduces atmospheric influence on the noble gas measurements. Comparison with laser ablation data shows that there is still some atmospheric contamination, suggesting that contamination begins on the seafloor. Two groups of samples have been identified based on their noble gas compositions: one group with their highest measured ratios similar to those of sample 2πD43 ($^{20}Ne/^{22}Ne$ of ~ 12.5, $^{40}Ar/^{36}Ar$ of ~ 27,000), and another group with lower maximum noble gas ratios ($^{20}Ne/^{22}Ne$ of 12.2, $^{40}Ar/^{36}Ar$ of 16,100) and higher argon concentrations. Based on these results, along with Cl/K and H_2O/Ce ratios and

preliminary lead, strontium and neodymium isotope data, it is suggested that these two groups of samples reflect separate eruptive events that originated from distinct mantle sources. This provides evidence for upper mantle heterogeneity at small scales and could imply that the mantle source with lower neon and argon isotopic ratios has been more influenced by recycling of atmospheric noble gases.

Keywords: popping rock, mid ocean ridge basalt, noble gases, Mid-Atlantic Ridge, heterogeneous mantle

I) Introduction

The isotopic and elemental compositions of mantle volatiles are key to understanding the origin and cycling of volatiles between the mantle and the atmosphere and Earth dynamics since the Hadean (e.g., Holland and Ballentine, 2006; Kurz et al., 2009; Moreira et al., 1998; Mukhopadhyay, 2012; Trieloff et al., 2000). However, the present-day volatile elemental composition of the mantle is difficult to determine because volatiles are sensitive to near-surface degassing (e.g., Burnard et al., 2003; Moreira and Kurz, 2013; Sarda and Moreira, 2002). This magmatic process is hard to quantify since it depends on several physicochemical conditions that are not well constrained. Nevertheless, it is considered that some rare samples did not suffer degassing, such as popping rocks (e.g., Sarda and Graham, 1990). Popping rocks are unusually gas-rich oceanic lava samples that pop after recovery from the seafloor due to vesicle gas decompression. Due to their high gas contents, they represent crucial samples for studying the volatile isotopic and elemental composition of the mantle and the associated heterogeneities (Javoy and Pineau, 1991; Moreira et al., 1998; Sarda and Graham, 1990).

Popping rocks have been found in only a few places, in particular mid-oceanic ridge basalts (MORBs) on the Mid-Atlantic Ridge at 36 °N (sample CH-DR11-315X, Hekinian et al., 1973; Pineau et al., 1976) and the well-studied sample 2πD43 near 14 °N (Bougault et al., 1988; Sarda and Graham, 1990). Due to its high gas content and vesicularity of 16 %, it is often assumed that sample 2πD43 did not suffer vesicle loss and is often considered as representative of the upper mantle noble gas isotopic and elemental compositions (Burnard et al., 1997; Kunz, 1999; Kunz et al., 1998; Moreira et al., 1998; Raquin et al., 2008; Sarda and Graham, 1990; Staudacher et al., 1989) and carbon abundance (Javoy and Pineau, 1991), despite its relative enrichment in incompatible elements (Bougault et al., 1988; Dosso et al.,

1991). Chavrit et al. (2014) suggested that such characteristics are more consistent with a process of bubble accumulation, given the higher number of big vesicles compared with other MORBs.

However, the location of sample 2πD43 on the Mid-Atlantic Ridge was not precisely known, because it was obtained by dredging, and the tectonic context could not be fully interpreted. A new cruise (AT33-03) was conducted in 2016 to find popping rocks in this area in order to better understand the formation of such gas-rich samples and the cycling of volatiles on Earth.

Basaltic glass samples are often contaminated by a seawater- or air-derived component, likely through cracks (Ballentine and Barfod, 2000; Roubinet and Moreira, 2018), which complicates noble gas interpretations. In this study, a new protocol was tested to recover the samples in anaerobic samplers, avoiding contact with air.

We report noble gas compositions of new popping rocks recovered in 2016 on the Mid-Atlantic Ridge determined both *via* step-crushing and laser ablation analyses. Laser ablation noble gas measurements have proved to be an effective technique to reduce atmospheric contamination issues (Raquin et al., 2008), so that results of laser ablation and step-crushing can be compared to evaluate the efficiency of the new anaerobic protocol and to assess the mechanisms of atmospheric contamination. The results are also compared with existing and new data for sample 2πD43, which was re-analyzed *via* laser ablation. These new data provide insight into isotopic and elemental heterogeneities of the mantle and the cycling of volatiles on Earth.

II) Samples and analytical procedure

2.1 AT33-03 cruise and geological settings

Cruise AT33-03 of *R/V Atlantis* took place in 2016 on the Mid-Atlantic Ridge and studied the area between 13°45' N and 14°06' N, with the aim of finding popping rocks and relating their occurrence to the tectonic setting (Jones et al., 2019; Parnell-Turner et al., 2018). Popping rock sample 2πD43 was recovered by dredging close to 13°46' N (Bougault et al., 1988) but the location on the ridge was not precisely known due to the uncertainty associated with dredging and navigation.

The southern part of the studied area, between 13°45' N and 13°52' N, is a non-transform discontinuity with limited magmatic activity, and topographically irregular flanks, whereas the northern part shows clear volcanic activity (Smith et al., 2008). There is an extinct oceanic core complex in the southern part (at ~ 13°50' N, 44°56' W, figure 1) as identified by Smith et al. (2008) and studied by Parnell-Turner et al. (2018), that is northeast of the approximate location of popping rock 2πD43 (Bougault et al., 1988).

High-resolution bathymetric maps of the seafloor were obtained via the autonomous underwater vehicle (AUV) *Sentry* and sampling was performed in-situ with the human occupied vehicle (HOV) *Alvin* (Jones et al., 2019; Parnell-Turner et al., 2018).

2.2 Samples and protocol on the ship

Five samples from the AT33-03 cruise were analyzed in this study (figure 1), by both step crushing and laser ablation for single vesicle analyses, samples AL4818-003, AL4820-036,

AL4820-041, AL4821-055 and AL4821-058 (abbreviated hereafter as 003, 036, 041, 055 and 058 respectively). Major and trace element compositions as well as major volatile contents (CO_2, H_2O, Cl, F, S) and averaged helium isotope ratios measured by crushing are presented elsewhere (Jones et al., 2019). These five samples are highly enriched in incompatible elements and have chondrite-normalized La/Sm ratios of about 1.8 (Jones et al., 2019), indicating that they represent E (enriched)-MORB. Samples 003, 036, 055 and 058 were identified as popping rocks because they visibly and audibly popped on the ship. Sample 041 was collected from an adjacent pillow mound and has intermediate vesicularity (4.4 % - 6 %, Jones et al. (2019) and table S2), but was not observed to pop on the ship. We also analyzed one piece of the popping rock sample 2πD43 with laser ablation to ensure that we were able to reproduce previous data (Moreira et al., 1998; Raquin et al., 2008).

In order to reduce atmospheric contamination of the glass samples for noble gas analyses, we tested a new protocol on the ship. Glass samples can be contaminated by air through cracks and opened vesicles (e.g., Ballentine and Barfod, 2000; Roubinet and Moreira, 2018) and this contaminant mixes with mantle gases when samples are crushed, which complicates noble gas interpretations. During sampling on the seafloor, two of the samples were recovered in sealed containers filled with ambient bottom-water. On the ship, the seawater was flushed out with nitrogen and the container was set inside a glove box filled with nitrogen. The glass from the sample could then be chipped away and stored into a closed stainless-steel tube, which is pumped until the pressure drops to ~10^{-5} - 10^{-6} mbar. These samples were never in contact with air. Samples 055 and 058 were recovered in these special sealed containers following this 'anaerobic' sampling protocol and were analyzed by step-crushing.

We also stored some glass samples (recovered in the sealed sea-floor containers and handled in a nitrogen atmosphere) in plastic bags that were pumped with a commercial culinary vacuum sealing machine to remove as much air as possible. These glass samples

were exposed to air for only a few minutes (1-2 min), prior to vacuum packaging. This was the case for pieces of samples 055 and 058 analyzed by laser ablation.

The other samples were recovered in open baskets on the HOV *Alvin* and were hence directly in contact with air after *Alvin* recovery. Some of them were also stored in the plastic bags and pumped 15-20 hours after *Alvin* recovery. This was the case for pieces of samples 003 and 036 analyzed by laser ablation.

2.3 Laser ablation analyses

Laser ablation noble gas analyses were conducted at Institut de Physique du Globe de Paris (IPGP). Pieces of samples 003, 036, 055 and 058 used for laser ablation were stored in plastic bags (Section 2.2) on the ship and were then put into the glove box filled with nitrogen in the IPGP laboratory. The piece of sample 041 used for laser ablation was not stored in vacuum and was therefore fully exposed to air.

Before laser ablation analyses, samples were removed from the glove box to be polished and then scanned via X-ray microtomography. This 3D imaging technique allows precise location of the intact bubbles before targeting with the laser for noble gas analyses. The tomography images (Figures S1, S2, S3 and S4) were acquired with a Bruker Skyscan 1173 at the Institute of Earth Sciences, University of Lausanne and the parameters used for the acquisitions are provided in Supplementary Information (Table S1). The protocols for sample preparation, image reconstruction and calculation of vesicularities (table S2) are described in Péron et al. (2016) and Péron et al. (2017). The four popping rock samples have estimated vesicularities between 9 % (sample 003) and 21 % (samples 036 and 055), whereas sample 041 has a vesicularity of 6 % (table S2). These estimates are a few percent lower or higher than those of Jones et al. (2019). This could be due to heterogeneity in vesicularity between

sub-samples, or it could also be an effect of image processing. In this study, we did not smooth the images, in order to preserve sample characteristics and to distinguish small cracks, even though smoothing refines vesicle contours and is useful for calculation of vesicularities (Péron et al., 2016). The vesicularity of sample 2πD43 was calculated to be 16 %, which is consistent with the values of 16% - 17% found by Sarda and Graham (1990) and Javoy and Pineau (1991).

Laser ablation noble gas analyses were conducted following a similar protocol as described by Péron et al. (2016) and Péron et al. (2017) and are summarized briefly here. After X-ray microtomography acquisition, samples were cleaned in ethanol and acetone baths and then with oxalic acid (1 %, at 60-80 °C) if iron-manganese crusts were observed. Samples were then loaded into the laser cell, which was baked at 100-150 °C for at least one month, to minimize line blanks, before starting laser ablation. Sample pieces used for laser ablation were thus exposed to air for several weeks. Laser ablation measurements were started as soon as the line blanks decreased to about 4.9×10^{-10} ccSTP of ^{4}He, 4.6×10^{-13} ccSTP of ^{22}Ne and 5.8×10^{-12} ccSTP of ^{36}Ar, and they kept decreasing thereafter.

The laser used is an argon fluoride (excimer) laser, ATLEX-300i instrument, of wavelength 193 nm and the pressure in the laser cell was monitored with a MKS Baratron® manometer. The pressure increase generated when reaching a bubble was calibrated with an air standard, which allows calculation of CO_2 abundances in the vesicles assuming that CO_2 is the major gas (Moore et al., 1977).

After a vesicle was breached by laser ablation, gases were purified with two Ti getters, one was heated to 800 °C for five minutes and then set to ambient temperature as the other step, before being trapped (except He) on a cold head at about 20 K. Noble gases were then analyzed on a Noblesse mass spectrometer (Nu instruments ©) (Supplementary Information). To correct for interferences on neon isotopes, as explained in Péron et al. (2017), we carried

out a scan of HF before introducing the neon into the mass spectrometer and then measured the CO_2 and ^{40}Ar signals during each cycle. The ionization ratios $^{40}Ar^{++}/^{40}Ar^{+}$ and CO_2^{++}/CO_2^{+} were determined on the Noblesse mass spectrometer to be 0.116 and 0.013 respectively during the analysis period (Figures S6, S7, S8 and S9).

As explained in Péron et al. (2016) and in Péron et al. (2017), laser ablation analyses are corrected with the matrix blanks (Tables S3 and S4). We analyzed the matrix gas composition after laser ablation of vesicle-free glass for a representative time. As described in Supplementary Information, matrix isotopic compositions are atmospheric and do not depend on the ablation time. We used a matrix blank that was measured just before or just after a vesicle for corrections. For the majority of the vesicles, the matrix blank contributions were less than 0.3 % for He and less than 30 % for Ne and Ar.

Two standards were used for laser ablation analyses (Supplementary Information), an air standard ($^{20}Ne/^{22}Ne$ = 9.80, $^{21}Ne/^{22}Ne$ = 0.029, $^{38}Ar/^{36}Ar$ = 0.188, $^{40}Ar/^{36}Ar$ = 295.5) and a mixed gas standard for He and Ne (Péron et al., 2016).

2.4 Step-crushing analyses

Step-crushing analyses were conducted at Woods Hole Oceanographic Institution (WHOI) on clean, centimeter-sized, glass fragments, typically 1-2 grams in size. Helium and neon were analyzed using a MAP 215-50 mass spectrometer in the WHOI Isotope Geochemistry Facility, as described by Kurz et al. (2005) and Kurz et al. (2009). The helium standard has a $^{3}He/^{4}He$ ratio of 8.35 Ra with ~ 5×10^{-9} cm^3 STP ^{4}He and was calibrated against air aliquots; air was used as the neon and argon standard ($1–2\times10^{-10}$ cm^3 STP neon). Crushing blanks are typically 1×10^{-11} cm^3 STP ^{4}He and 2×10^{-12} cm^3 STP ^{20}Ne. Interferences at masses 20 and 22 were minimized with a charcoal trap held at liquid nitrogen temperatures

within the flight tube volume. Corrections for interferences from $^{40}Ar^{++}$ and CO_2^{++} on ^{20}Ne and ^{22}Ne peaks were made using measurements at masses 40 and 44; no correction was necessary for interferences from $H_2{}^{18}O$ and HF because peaks at masses 18 and 19 were negligible. The ratios of doubly charged/singly charged contributions, on masses 20 and 22, for masses 40 and 44 were typically 0.23 and 0.012; the 40 and 44 peaks were generally small relative to the sample gas, making these corrections unimportant (mass 40 and 44 peaks were typically less than 100 counts per second during these measurements). Stated uncertainties are 1 sigma, calculated as quadrature sum of estimated analytical uncertainties. Argon isotopes were measured using a dedicated Quadrupole Mass Spectrometer (Hiden), attached to the same extraction line. Helium, neon and argon were separated using two automated cryogenic traps, one nude stainless steel and one charcoal. All measurements were made by crushing *in vacuo*, using well established procedures (e.g., Kurz et al., 2009). The quantities of gas introduced into the extraction line and mass spectrometers were controlled by capacitance manometry, followed by a pre-measurement with a quadrupole mass spectrometer, and volumetric splitting as necessary to match sample size with standard size. Pre-gettering capacitance manometry measurements were used to calculate $CO_2/^3He$ ratios (table 3), assuming that CO_2 constitutes most of the volatiles released by crushing (Moore et al., 1977). Noble gas concentrations are so high in these samples that they could be measured many times by crushing.

III) Results

3.1 Comparison of laser ablation and step-crushing data

Of the 27 individual vesicles analyzed by laser ablation, most of the data are similar to the highest neon and argon isotopic values obtained by step-crushing (Figures 2, 3, 4, 5 and tables 1, 2 and 3). Overall, there is excellent agreement between the highest step-crushing values and most laser ablation measurements.

Six vesicles show anomalous variations in elemental and isotopic compositions, compared to the bulk crushing measurements, which are not easily explained by a single process. Vesicles V5 of sample 055 and V2 of sample 2πD43 have strongly fractionated He, Ne and Ar composition. The neon and argon isotopic ratios are close to air, $^{3}He/^{22}Ne$ and $^{4}He/^{40}Ar^{*}$ ratios are close to 0 and they have lower $^{22}Ne/^{36}Ar$ ratios than for other vesicles from the same samples (table 2, figures 2, 3, 4 and 5). Pressure increases were detected by manometry (on laser ablation) in both cases, but are much lower than expected given the vesicle volumes (table 1). Vesicle V4 of sample 041 also yielded a lower-than-expected pressure jump and clearly shows He, Ne and Ar loss, based on very low He, Ne and Ar contents in comparison with other vesicles of similar sizes (table 1). Vesicle V2 of sample 058 has clearly lost helium, based on low ^{4}He content and extremely low $^{3}He/^{22}Ne$ and $^{4}He/^{40}Ar^{*}$, but has a neon and argon isotopic compositions similar to the other vesicles of sample 058 (tables 1 and 2). Vesicle V8 of sample 036 seems to have lost helium (based on lower $^{4}He/^{40}Ar^{*}$, table 2) and was too small to properly measure the neon (table 2).

Vesicle V2 of sample 055 also shows some He loss (lower $^{4}He/^{40}Ar^{*}$ of 0.93, relative to all other measurements, a higher $CO_2/^{3}He$ ratio and a slightly higher $^{3}He/^{4}He$ ratio) but has

neon and argon isotopic ratios similar to the other vesicles of sample 055 and so the neon and argon compositions are used along with data from other vesicles in section 3.3.

No clear cracks were identified close to the six anomalous bubbles on the X-ray microtomography images but the image resolutions are insufficient to detect cracks smaller than around 10 µm (table S1). The processes that fractionated the noble gas abundances and isotopic compositions in these six vesicles are not known, but these data are not interpreted as magmatic values.

It is also interesting to note that vesicle V9 of sample 036 is a very big vesicle that may have formed by coalescence of smaller vesicles, due to its irregular (non-spherical) shape (Figure S3). Vesicle V9 gas contents (CO_2, He, Ne, Ar) are lower than expected given its volume but its elemental and isotopic ratios are similar to that of the other vesicles, which could be due to the coalescence process.

3.2 CO_2, helium and radiogenic argon $^{40}Ar^*$

Excluding the six anomalous vesicles mentioned in section 3.1, vesicles from samples 003, 036, 055 and 058 have a mean $CO_2/^3He$ ratio of 3.35 (± 0.17) x10^9 (1σ) (table 2), which agrees well with the value of 3.08 (± 0.23) x10^9 from bulk step-crushing (table 3). Vesicles from sample 041 have a mean $CO_2/^3He$ ratio of 3.01 (± 0.22) x10^9 (1σ) (2.53 (± 0.21) x10^9 with step-crushing) and vesicles of sample 2πD43 a mean value of 3.17 (± 0.23) x10^9 (1σ). These values are higher than the estimated median value of 2.2 x10^9 (Marty and Tolstikhin, 1998) or the recent average MORB estimate of 1.67 (± 0.21) x10^9 (Tucker et al., 2018). They are similar to the value estimated for E-MORB of 3.3 (± 1.1) x10^9 (or 4.5 (± 1.3) x10^9 corrected for fractional degassing) (Marty and Tolstikhin, 1998). This is consistent with these samples being E-MORB, as also suggested by their major and trace element compositions

(Jones et al., 2019) and by the preliminary Pb, Sr, Nd data (section 4.3 and table S5). The new data therefore support a higher $CO_2/^3He$ for E-MORB than for N (normal)-MORB.

The helium isotopic compositions are quite homogenous among all the vesicles, excluding the six anomalous vesicles, which have $^3He/^4He$ both lower and higher than other measurements (Table 4). The mean $^3He/^4He$ ratio is 8.33 ± 0.17 Ra (1σ) for samples 003, 036, 055 and 058, with Ra indicating the atmospheric $^3He/^4He$ ratio ($1.384x10^{-6}$, (Clarke et al., 1976)). The mean $^3He/^4He$ ratio is 8.48 ± 0.11 Ra (1σ) for sample 041 and 8.48 ± 0.15 Ra (1σ) for sample 2πD43. The averages are lower, but within uncertainties for step-crushing data, with $^3He/^4He$ ratio of 8.16 ± 0.18 Ra (1σ) for samples 003, 036, 055 and 058 and 8.32 ± 0.13 Ra (1σ) for sample 041. The $^3He/^4He$ from the six anomalous vesicles range from 0.98 to 10 Ra, suggesting extensive isotope fractionation by helium migration into and out of the vesicles.

Except for the six anomalous vesicles, the mean vesicle $^4He/^{40}Ar^*$ ratio obtained by laser ablation is 1.14 ± 0.04 (1σ) for samples 003, 036, 055 and 058, whereas it is 1.39 ± 0.06 for sample 041 and 1.34 ± 0.05 for sample 2πD43. The average values with step-crushing measurements are 1.06 ± 0.07 (1σ) for samples 003, 036, 055 and 058 and 1.32 ± 0.07 (1σ) for sample 041. The laser ablation and step-crushing values are therefore in good agreement.

3.3 Neon and argon isotopic ratios

Figures 2 and 3 show the neon and argon isotopic data for step-crushing and laser ablation measurements. Sample 041 has neon and argon isotopic compositions similar to sample 2πD43 (green dots and results from Moreira et al. (1998)) with maximum $^{20}Ne/^{22}Ne$ values of around 12.5, $^{21}Ne/^{22}Ne$ of approximately 0.060 and $^{40}Ar/^{36}Ar$ of 26,000-27,000.

The other samples (003, 036, 055 and 058) show distinctly lower (maximum) neon and argon isotopic ratios. The mean $^{20}Ne/^{22}Ne$ ratios are 12.17 ± 0.06 (1σ) for step-crushing (steps with $^{20}Ne/^{22}Ne$ ratio > 12) and 12.24 ± 0.22 (1σ) for single vesicle analyses (vesicles with $^{20}Ne/^{22}Ne$ ratio > 12). Similarly, $^{21}Ne/^{22}Ne$ for crushing steps and laser analyses (each restricted to $^{20}Ne/^{22}Ne$ ratio > 12) display ratios of around 0.0567 and 0.0578 respectively, and the mean $^{40}Ar/^{36}Ar$ ratio is 16,088 ± 262 (1σ) for the single vesicle analyses. The latter value is consistent with the highest $^{40}Ar/^{36}Ar$ ratios obtained by step-crushing. It is important to note that strong CO_2 memory effects in the mass spectrometer were observed on the neon analysis of vesicle V4 from sample 2πD43 because it was analyzed just after vesicle V3 and so ^{22}Ne was poorly corrected for CO_2, which makes this data point unreliable (table 2 and figure S7). Vesicle V2 of sample 041 was too small to measure reliable neon isotopic ratios.

In figure 3, it is interesting to note that samples 055 and 058, recovered in the anaerobic samplers, plot on a hyperbola with a higher curvature r (r is $(^{36}Ar/^{22}Ne)_{air\ or\ seawater}/(^{36}Ar/^{22}Ne)_{mantle}$), compared with sample 003 (which was fully air exposed). Vesicles V5 of sample 055 and V2 of sample 2πD43 plot on a hyperbola with a lower curvature (figure 3), similar to that suggested by Raquin et al. (2008).

3.4 Elemental ratios

Figures 4 and 5 present the two elemental ratios $^{3}He/^{22}Ne$ and $^{36}Ar/^{22}Ne$ plotted against $^{20}Ne/^{22}Ne$. The $^{3}He/^{22}Ne$ and $^{36}Ar/^{22}Ne$ ratios of sample 041 are similar to sample 2πD43 and are about 4.52 ± 0.09 (1σ, steps with $^{20}Ne/^{22}Ne$ ratio > 12) and 12.10 ± 0.34 (1σ, vesicles) respectively. The other samples (003, 036, 055 and 058) show different $^{3}He/^{22}Ne$ and $^{36}Ar/^{22}Ne$ ratios of 4.04 ± 0.19 (1σ, steps with $^{20}Ne/^{22}Ne$ ratio > 12) and 23.7 ± 2.3 (1σ, vesicles) respectively.

Most of the vesicle data have higher $^{3}He/^{22}Ne$ ratios than the highest step-crushing data but the uncertainties are relatively large and so the step-crushing data seem to best determine the $^{3}He/^{22}Ne$ ratio.

In figure 5 and S5 in Supplementary Information, step-crushing data for sample 003 suggest mixing between air and a mantle component, whereas step-crushing data for samples 041, 055 and 058 show mixing with a seawater-derived component, based on the different abundance ratios. Vesicles V5 of sample 055 and V2 of sample 2πD43 show mixing between air and seawater.

IV) Discussion

4.1 Sample contamination processes and the use of laser ablation measurements

Our results suggest that the protocol used to collect and analyze anaerobic samples (those without contact with air) is effective in reducing shallow air contamination. It is particularly evident in the case of neon (figures 2, 3, 4, 5 and S5), as observed in step-crushing data for anaerobic samples 055 and 058 compared with sample 003, which was fully exposed to air. The majority of the crushing steps for samples 055 and 058 are close to the highest values, in contrast to the crush steps for sample 003. Sample 041 was also fully exposed to air. The crushing measurements of sample 041 show limited neon and argon contamination, which could be related to its lower vesicularity (table S2). This limited sample suite shows promise for the method, but additional testing on more samples is needed.

As shown in figures 5 and S5, step-crushing data for samples 041, 055 and 058 show mixing with a seawater-derived component rather than with air, as is observed for sample 003, even if most of the steps for samples 041, 055 and 058 show limited contamination.

Interaction with a seawater-derived component is also suggested by the mixing hyperbola of higher curvature (r ~ 5) in figure 3 because the seawater $^{36}Ar/^{22}Ne$ ratio is higher than that of air (figure 5). This suggests that seawater contamination begins on the seafloor during or after emplacement, likely through cracks (Ballentine and Barfod, 2000), and that air quickly replaces this seawater-derived component after collection. Indeed, sample 003, which was fully air exposed after collection and has a high vesicularity, is more influenced by air than seawater (figures 3 and 5), in contrast to the anaerobically collected samples. Additional results from this new protocol will be provided in a subsequent paper.

The excellent agreement between the laser ablation and the highest step-crushing data (section 3.1) suggests that both techniques are effective in determining the mantle composition. A few laser ablation data show variability from the step-crushing results (figures 2, 3, 4, 5), highlighting that processes of contamination are complex, as also discussed by Roubinet and Moreira (2018). Hence, laser ablation analyses represent a powerful method for better understanding this contamination process compared to step-crushing. It is important to note that some bubbles could not be analyzed, either because the laser spot was positioned incorrectly or more likely because no pressure increase was detected. The latter case would indicate that these bubbles were completely contaminated with atmosphere/seawater gases, maybe through cracks, prior to analysis and that no magmatic CO_2 was left. No pressure jump can be detected with our system if a bubble is at atmospheric pressure.

As mentioned in section 3.3, vesicles V5 of sample 055 and V2 of sample 2πD43 show mixing between air and seawater given their $^{22}Ne/^{36}Ar$ ratios, and plot on the hyperbola with a low curvature in figure 3. Vesicle V2 of sample 058 and vesicle V4 of sample 041 also seem to plot on hyperbolas with low curvatures ($r < 1$). Other vesicles (V2 and V3 of sample 003, V2 of sample 036, V1 and V4 of sample 058) like V2 of sample 058 also seem to have a $^{20}Ne/^{22}Ne$ ratio slightly lower than 12 and fall on the hyperbola with a low curvature in figure

405 3. We can exclude analytical issues for these bubbles (Supplementary Information and figures
406 S6, S7, S8, S9). All these vesicles are slightly to heavily contaminated by air/seawater or have
407 lost gases (e.g., V4 of sample 041). The fact that they all fall on hyperbolas with low
408 curvatures suggests that they were contaminated in different proportions. This contamination
409 process may occur through small cracks that cannot be observed on X-ray microtomography
410 images given the image resolutions (Table S1).

411 For vesicles that have lower $^{20}Ne/^{22}Ne$ ratios (V2 and V3 of sample 003, V2 of sample
412 036, V1 and V4 of sample 058) and also for vesicle V2 of sample 058 with a fractionated He
413 isotopic ratio ($^{3}He/^{4}He$ of 5.60 ± 0.37 Ra), it is important to note that they contain CO_2 in the
414 expected amount given their volumes. No influence of the ablation depth below the sample
415 polished surface can be observed. All these observations are hard to reconcile. When bubbles
416 are only slightly contaminated, helium should not be easily affected because there is so little
417 He in air and seawater. Only vesicle V2 of sample 058 seems to have a higher $^{36}Ar/^{22}Ne$ ratio
418 (figure 5). Previous studies have noted that the complexities of the isotopic and abundance
419 ratio mixing trends require several different processes (e.g., Burnard et al., 2003).

420 The two strongly fractionated vesicles, V5 of sample 055 and V2 of sample 2πD43, with
421 low CO_2 abundances (table 1), may be connected to bigger cracks than the other vesicles and
422 so CO_2 could have escaped with noble gases. Seawater-derived noble gases could enter the
423 bubbles, followed by atmospheric noble gases when samples are exposed to air after recovery.
424 This may be a relatively slow process because the two vesicles still show influence of
425 seawater-derived noble gases, consistent with contamination via very small cracks.

426 Vesicle V4 of sample 041 seems to be a special case because it has lost CO_2, He, Ne and
427 Ar but does not have atmospheric isotopic ratios like V5 of sample 055 and V2 of sample
428 2πD43. This suggests that this piece of sample 041 was degassed.

To summarize, the new protocol to collect samples anaerobically appears to reduce air/seawater contamination and is promising for future missions to better characterize mantle composition. Results from this new protocol highlight that contamination starts on the seafloor and that air replaces this seawater component relatively quickly after recovery. However, as shown by the laser ablation data, the contamination processes are complex and not yet fully understood.

4.2 The $^{4}He/^{40}Ar^{*}$ ratio

The $^{4}He/^{40}Ar^{*}$ ratio is a useful tracer of degassing. Indeed, both ^{4}He and $^{40}Ar^{*}$ ($^{40}Ar^{*}$ is radiogenic ^{40}Ar, calculated by subtracting the atmospheric contribution assuming ^{36}Ar is fully atmospheric) are radiogenic isotopes produced in the mantle, with an estimated production ratio of 2 to 5 (Moreira and Kurz, 2013). This production ratio is a function of assumed mantle K, Th, and U abundances and the assumption of a closed system evolution, so there is inherent uncertainty, but serves as a useful reference for mantle values and the influence of degassing. Since argon is less soluble in melts than helium, the $^{4}He/^{40}Ar^{*}$ ratio would increase if a magma was degassed (Moreira and Kurz, 2013; Sarda and Moreira, 2002).

As indicated in table 2 and table 3, the $^{4}He/^{40}Ar^{*}$ ratios are lower than the production ratio. The $^{4}He/^{40}Ar^{*}$ ratio of 1.37 ± 0.05 for samples 041 and 2πD43 obtained here is consistent with previous studies of the popping rock 2πD43, which found values of 1.36 (Javoy and Pineau, 1991), 1.5 ± 0.1 (Moreira et al., 1998) and 1.4 ± 0.1 (Raquin et al., 2008). Burnard et al. (1997) determined a lower value of 0.99 but Raquin et al. (2008) suggested that this could be due to different extent of degassing between vesicles, or that Burnard et al. (1997) did not correct argon isotopic ratios for mass discrimination. Staudacher et al. (1989) calculated a higher $^{4}He/^{40}Ar^{*}$ ratio, between 2.08 and 2.72, for sample 2πD43.

The low $^{4}He/^{40}Ar^{*}$ ratio of the popping rocks is enigmatic. Lower $^{4}He/^{40}Ar^{*}$ cannot be explained via degassing because one would expect $^{4}He/^{40}Ar^{*}$ ratios higher than the production ratio due to lower Ar solubility (Moreira and Kurz, 2013). In case of very low vesicularity, vesicles could potentially have low $^{4}He/^{40}Ar^{*}$ ratios because most of the gas remains in the melt and argon is less soluble than helium (Sarda and Moreira, 2002), leading to bubbles enriched in argon. But this is not the case for the highly vesicular samples analyzed in this study. It was suggested that popping rocks reflect a process of bubble accumulation (Chavrit et al., 2014; Jones et al., 2019). Such a process should not influence the $^{4}He/^{40}Ar^{*}$ ratio, unless first-generated vesicles, with lower $^{4}He/^{40}Ar^{*}$ ratios due to the lower solubility of argon in melts, are accumulated. Another explanation would be diffusive loss of helium from the magma before vesiculation since helium diffuses faster than argon.

An interesting point is that samples 003, 036, 055 and 058 have systematically (both laser ablation and step-crushing measurements) lower $^{4}He/^{40}Ar^{*}$ ratios than the samples 041 and 2πD43. There is no relation between the vesicularities and the $^{4}He/^{40}Ar^{*}$ ratios (tables S2 and 2). This difference in the $^{4}He/^{40}Ar^{*}$ ratio could be related to the enrichment in argon observed in samples 003, 036, 055 and 058 compared with samples 041 and 2πD43 (figure 6): for a same vesicle volume, samples with lower $^{4}He/^{40}Ar^{*}$ ratio show higher ^{36}Ar content. Such a trend is not observed for helium and neon. This could reflect that the magmatic source of samples 003, 036, 055 and 058 is enriched in argon compared with the source of samples 041 and 2πD43.

4.3 Upper mantle noble gas isotopic and elemental compositions

One goal of this study is to better characterize upper mantle noble gas compositions. The difference in isotopic and elemental compositions between samples 003, 036, 055 and 058 and samples 041 and 2πD43 is significant (figures 2, 3, 4 and 5).

One hypothesis is that samples 003, 036, 055 and 058 represent assimilation of altered oceanic crust or of sedimentary material, leading to lower $^{40}Ar/^{36}Ar$, $^{20}Ne/^{22}Ne$ and $^{22}Ne/^{36}Ar$ ratios. The Cl/K and H_2O/Ce ratios are useful tracers of assimilation of hydrothermally altered material and seawater-derived components (Dixon et al., 2002; Michael and Cornell, 1998; Stroncik and Niedermann, 2016). However, all the samples have Cl/K ratios in the range 0.050-0.054 and H_2O/Ce ratios between 160 and 174 (table 3, Jones et al., 2019), which is in the range of 0.05-0.08 for Cl/K suggested for uncontaminated E-MORB (Michael and Cornell, 1998) and is typical of MORB for H_2O/Ce (Dixon et al., 2002). Therefore, assimilation of seawater-altered oceanic crust during the transport to the surface seems not to be reflected in the Cl/K and H_2O/Ce ratios; even though, noble gas ratios (e.g., $^{40}Ar/^{36}Ar$, $^{22}Ne/^{36}Ar$) can be more sensitive to these processes than Cl/K as shown by Stroncik and Niedermann (2016).

The popping rock samples 003, 036, 055 and 058 exhibit very similar noble gas compositions, whereas one could expect that they would have been contaminated to various degrees, if they were influenced by crustal contamination. As discussed in section 4.2, samples are unlikely to be degassed given their low $^{4}He/^{40}Ar^{*}$ ratios. However, the magmatic source of samples 003, 036, 055 and 058 seems to be enriched in argon (figure 6 and section 4.2) compared with the magma of samples 041 and 2πD43.

Preliminary lead, strontium and neodymium isotopic compositions for samples from the popping rock area show measurable differences (table S5), providing independent evidence

504 that these samples originate from two distinct mantle sources. The $^{206}Pb/^{204}Pb$ ratio is 18.962
505 for sample 041 and 19.026 ± 0.002 for samples 003, 055 and 058, which is well beyond
506 measurement uncertainty (section S5 in Supplementary Information). Small but measurable
507 differences are also observed in Sr and Nd isotopes. The mantle source with low $^{20}Ne/^{22}Ne$,
508 $^{40}Ar/^{36}Ar$ and $^{22}Ne/^{36}Ar$ ratios (samples 003, 036, 055, 058) has more radiogenic lead than
509 sample 041. Sample 041 was collected from the easternmost location, potentially indicating a
510 geographic boundary. Further measurements are ongoing on a larger set of samples from the
511 area and will be published elsewhere.

512 The popping rock area (figure 1) is part of the strong geochemical (E-MORB) anomaly
513 identified at 14° N on the Mid-Atlantic Ridge, devoid of plume influence (Bougault et al.,
514 1988; Dosso et al., 1991; Hémond et al., 2006). Here, the preliminary Pb, Nd and Sr data
515 show that the upper mantle is heterogeneous at a much smaller scale. All the samples
516 analyzed in this study from the 2016 cruise (figure 1) have indistinguishable major and trace
517 element compositions but distinct Pb, Sr and Nd isotopic compositions, along with different
518 elemental and isotopic noble gas compositions (in particular distinct $^{20}Ne/^{22}Ne$, $^{40}Ar/^{36}Ar$,
519 $^{22}Ne/^{36}Ar$ and $^{4}He/^{40}Ar^{*}$). Several studies suggested that seawater noble gases (Ne, Ar, Kr,
520 Xe) could be recycled into the mantle through incorporation into hydrated minerals of the
521 subducted oceanic lithosphere despite their inertness (e.g., Holland and Ballentine, 2006;
522 Kendrick et al., 2018; Smye et al., 2017). Therefore, the mantle source of samples 003, 036,
523 055 and 058 could have been more affected by recycling of oceanic crust and so by noble gas
524 recycling, leading to a more radiogenic lead isotopic composition, argon enrichment and
525 lower $^{20}Ne/^{22}Ne$, $^{40}Ar/^{36}Ar$ and $^{22}Ne/^{36}Ar$.

526 Several studies have shown that the upper mantle is chemically heterogeneous on different
527 scales (e.g., Agranier et al., 2005; Allègre and Turcotte, 1986; Bougault et al., 1988; Chavrit
528 et al., 2014; Dosso et al., 1991; Graham et al., 1992; Hémond et al., 2006; Parai et al., 2012;

529 Tucker et al., 2012; Wilson et al., 2013). Recycling of atmospheric noble gases was invoked
530 to account for some of these heterogeneities (e.g., Parai et al., 2012; Sarda et al., 1999; Tucker
531 et al., 2012). Based on lead-argon isotopic correlations observed for MORBs from the
532 Atlantic ocean, Sarda et al. (1999) suggested that atmospheric noble gases are recycled into
533 the mantle and that argon would be a tracer of subducted material which shows $^{40}Ar/^{36}Ar$
534 close to air. Tucker et al. (2012) discussed heterogeneities observed in the noble gas
535 compositions of MORBs from the equatorial Mid-Atlantic Ridge, in particular large $^{40}Ar/^{36}Ar$
536 variations despite constant helium and neon isotopic compositions, which could also be partly
537 related to atmospheric noble gas recycling.

538 Based on these new data as well as on recent studies and compilations (Moreira, 2013;
539 Parai et al., 2012; Tucker et al., 2012), it seems that the highest (measurable) noble gas
540 isotopic ratios for the MORB mantle devoid of plume influence are 12.5 for $^{20}Ne/^{22}Ne$ and
541 30,000 for $^{40}Ar/^{36}Ar$. Lower maximum values (e.g., excluding shallow atmospheric
542 contamination) for these ratios could be related to interaction with a HIMU-plume component
543 (e.g., Tucker et al., 2012) and/or to different degrees of incorporation of recycled material in
544 mantle sources in the context of a marble-cake mantle (Agranier et al., 2005; Allègre and
545 Turcotte, 1986). Therefore, the noble gas isotopic composition of popping rock 2πD43 can be
546 considered as a reference for the upper mantle, even if this sample is an E-MORB (Bougault
547 et al., 1988; Dosso et al., 1991). A better understanding of the popping rock $^{4}He/^{40}Ar^{*}$ ratios
548 (section 4.2) is needed to constrain the upper mantle elemental noble gas ratios.

549 One explanation for the new observations is that recycled oceanic lithosphere into the
550 mantle can introduce small-scale heterogeneities, in particular for the noble gas elemental and
551 isotopic composition. A detailed study of the lithophile element and noble gas isotopic
552 compositions on a larger set of samples from the popping rock area will further constrain the
553 extent and scale of these heterogeneities.

V) Conclusion

Determining the volatile isotopic and elemental compositions of the mantle is crucial to better understand volatile cycling on Earth. Undegassed MORB, such as popping rocks, represent important samples to address these issues. We analyzed the noble gas compositions of five samples from the cruise AT33-03 on the Mid-Atlantic Ridge, four of which were popping rocks, with step-crushing and laser ablation, as well as the popping rock 2πD43 that was recovered in the same area in 1985.

A new protocol was tested to recover lavas with anaerobic samplers. It seems very efficient to reduce sample contamination, but the presence of a seawater- or air-derived component is still observed, suggesting that samples start being contaminated after eruption on the seafloor through cracks and opened vesicles and that air replaces this seawater component after recovery. This highlights that contamination processes are complex and that this contaminant is hard to remove (Ballentine and Barfod, 2000; Roubinet and Moreira, 2018).

Four samples (003, 036, 055 and 058) show distinct neon and argon isotopic and elemental compositions ($^{20}Ne/^{22}Ne$ of about 12.2 and $^{40}Ar/^{36}Ar$ of about 16,100) compared with sample 2πD43, whereas sample 041, the easternmost sample studied, has a composition similar to the popping rock 2πD43 ($^{20}Ne/^{22}Ne$ of 12.5 and $^{40}Ar/^{36}Ar$ of 27,000). The two groups of samples also have distinct $^{4}He/^{40}Ar^{*}$ ratios, which is consistent with the source of samples 003, 036, 055 and 058 being enriched in argon compared with the source of samples 041 and 2πD43 based on laser ablation data.

Preliminary lead, strontium and neodymium isotopic compositions indicate that these two groups of samples were produced by separate eruptive events from two distinct mantle sources. This provides evidence for upper mantle heterogeneity at small scale. The mantle

source of the samples with lower neon and argon isotopic ratios could have been affected by recycled oceanic crust and by recycled atmospheric noble gases, in a context of a marble-cake mantle (Allègre and Turcotte, 1986).

Acknowledgements

We thank Sujoy Mukhopadhyay and an anonymous reviewer for their insightful comments that helped improving this contribution as well as Tamsin Mather for editorial handling and constructive comments. Javier Escartín is greatly thanked for assistance with cruise planning and for his constructive comments on the first versions of this paper. We thank Dan Fornari and the rest of the science team for their excellent work at sea. The authors thank the captain and the crew of the *R/V Atlantis*, the AUV *Sentry* team, and the HOV *Alvin* team, for their invaluable help during the cruise. The authors are also grateful to Déborah Chavrit for fruitful discussions. The cruise and the WHOI noble gas measurements were supported by NSF OCE-1259218. S.P. acknowledges the financial support from the L'Oréal-UNESCO *For Women in Science* 2017 fellowship.

References

Agranier, A., Blichert-Toft, J., Graham, D.W., Debaille, V., Schiano, P., Albarède, F., 2005. The spectra of isotopic heterogeneities along the mid-Atlantic Ridge. Earth and Planetary Science Letters 238, 96-109.

Allègre, C.J., Turcotte, D., 1986. Implications of a two-component marble-cake mantle. Nature 323, 123-127.

Ballentine, C., Barfod, D., 2000. The origin of air-like noble gases in MORB and OIB. Earth and Planetary Science Letters 180, 39-48.

Bougault, H., Dmitriev, L., Schilling, J.-G., Sobolev, A., Joron, J.-L., Needham, H.D., 1988. Mantle heterogeneity from trace elements: MAR triple junction near 14°N. Earth and Planetary Science Letters 88, 27-36.

Burnard, P., Graham, D., Turner, G., 1997. Vesicle-specific noble gas analyses of "popping rock": implications for primordial noble gases in the Earth. Science 276, 568-571.

Burnard, P., Harrison, D., Turner, G., Nesbitt, R., 2003. Degassing and contamination of noble gases in Mid-Atlantic Ridge basalts. Geochemistry Geophysics Geosystems 4.

Chavrit, D., Humler, E., Grasset, O., 2014. Mapping modern CO_2 fluxes and mantle carbon content all along the mid-ocean ridge system. Earth and Planetary Science Letters 387, 229-239.
Clarke, W.B., Jenkins, W.J., Top, Z., 1976. Determination of tritium by mass spectrometric measurement of ^{3}He. The International Journal of Applied Radiation and Isotopes 27, 512-522.
Dixon, J.E., Leist, L., Langmuir, C., Schilling, J.-G., 2002. Recycled dehydrated lithosphere observed in plume-influenced mid-ocean-ridge basalt. Nature 420, 385.
Dosso, L., Hanan, B.B., Bougault, H., Schilling, J.-G., Joron, J.-L., 1991. Sr-Nd-Pb geochemical morphology between 10° and 17°N on the Mid-Atlantic Ridge: A new MORB isotope signature. Earth and Planetary Science Letters 106, 29-43.
Graham, D.W., Jenkins, W.J., Schilling, J.G., Thompson, G., Kurz, M.D., Humphris, S., 1992. Helium isotope geochemistry of mid-ocean ridge basalts from the South Atlantic. Earth and Planetary Science Letters 110, 133-147.
Hekinian, R., Chaigneau, M., Cheminee, J.L., 1973. Popping Rocks and Lava Tubes from the Mid-Atlantic Rift Valley at 36° N. Nature 245, 371-373.
Hémond, C., Hofmann, A.W., Vlastélic, I., Nauret, F., 2006. Origin of MORB enrichment and relative trace element compatibilities along the Mid-Atlantic Ridge between 10° and 24°N. Geochemistry, Geophysics, Geosystems 7.
Holland, G., Ballentine, C.J., 2006. Seawater subduction controls the heavy noble gas composition of the mantle. Nature 441, 186-191.
Javoy, M., Pineau, F., 1991. The volatiles record of a « popping » rock from the Mid-Atlantic Ridge at 14°N : chemical and isotopic composition of gas trapped in the vesicles. Earth and Planetary Science Letters 107, 598-611.
Jones, M.R., Wanless, V.D., Soule, S.A., Kurz, M.D., Mittelstaedt, E., Fornari, D.J., Curtice, J., Klein, F., Le Roux, V., Brodsky, H., Péron, S., Schwartz, D.M., 2019. New constraints on mantle carbon from Mid-Atlantic Ridge popping rocks. Earth and Planetary Science Letters 511, 67-75.
Kendrick, M.A., Scambelluri, M., Hermann, J., Padrón-Navarta, J.A., 2018. Halogens and noble gases in serpentinites and secondary peridotites: Implications for seawater subduction and the origin of mantle neon. Geochimica et Cosmochimica Acta 235, 285-304.
Kunz, J., 1999. Is there solar argon in the Earth's mantle? Nature 399, 649-650.
Kunz, J., Staudacher, T., Allègre, C.J., 1998. Plutonium-Fission Xenon Found in Earth's Mantle. Science 280, 877-880.
Kurz, M.D., Curtice, J., Fornari, D., Geist, D., Moreira, M., 2009. Primitive neon from the center of the Galápagos hotspot. Earth and Planetary Science Letters 286, 23-34.
Kurz, M.D., Moreira, M., Curtice, J., Lott III, D.E., Mahoney, J.J., Sinton, J.M., 2005. Correlated helium, neon, and melt production on the super-fast spreading East Pacific Rise near 17°S. Earth and Planetary Science Letters 232, 125-142.
Marty, B., Tolstikhin, I.N., 1998. CO2 fluxes from mid-ocean ridges, arcs and plumes. Chemical Geology 145, 233-248.
Michael, P.J., Cornell, W.C., 1998. Influence of spreading rate and magma supply on crystallization and assimilation beneath mid-ocean ridges: Evidence from chlorine and major element chemistry of mid-ocean ridge basalts. Journal of Geophysical Research: Solid Earth 103, 18325-18356.
Moore, J.G., Batchelder, J.N., Cunningham, C.G., 1977. CO_2-filled vesicles in mid-ocean basalt. Journal of Volcanology and Geothermal Research 2, 309-327.

660 Moreira, M., 2013. Noble gas constraints on the origin and evolution of Earth's volatiles.
661 Geochemical Perspectives 2, 229-403.
662 Moreira, M., Kunz, J., Allègre, C.J., 1998. Rare gas systematics on popping rock : estimates
663 of isotopic and elemental compositions in the upper mantle. Science 279, 1178-1181.
664 Moreira, M.A., Kurz, M.D., 2013. Noble Gases as Tracers of Mantle Processes and
665 Magmatic Degassing, in: Burnard, P. (Ed.), The Noble Gases as Geochemical Tracers.
666 Springer Berlin Heidelberg, pp. 371-391.
667 Mukhopadhyay, S., 2012. Early differentiation and volatile accretion recorded in deep
668 mantle Neon and Xenon. Nature 486, 101-104.
669 Ozima, M., Podosek, F.A., 2002. Noble Gas Geochemistry. Cambridge University Press.
670 Parai, R., Mukhopadhyay, S., Standish, J.J., 2012. Heterogeneous upper mantle Ne, Ar and
671 Xe isotopic compositions and a possible Dupal noble gas signature recorded in basalts
672 from the Southwest Indian Ridge. Earth and Planetary Science Letters 359-360, 227-
673 239.
674 Parnell-Turner, R.E., Mittelstaedt, E., Kurz, M.D., Jones, M.R., Soule, S.A., Klein, F.,
675 Wanless, V.D., Fornari, D.J., 2018. The Final Stages of Slip and Volcanism on an Oceanic
676 Detachment Fault at 13° 48′ N, Mid-Atlantic Ridge. Geochemistry, Geophysics,
677 Geosystems 0.
678 Péron, S., Moreira, M., Colin, A., Arbaret, L., Putlitz, B., Kurz, M.D., 2016. Neon isotopic
679 composition of the mantle constrained by single vesicle analyses. Earth and Planetary
680 Science Letters 449, 145-154.
681 Péron, S., Moreira, M., Putlitz, B., Kurz, M.D., 2017. Solar wind implantation supplied light
682 volatiles during the first stage of Earth accretion. Geochemical Perspectives Letters 3,
683 151-159.
684 Pineau, F., Javoy, M., Bottinga, Y., 1976. $^{13}C/^{12}C$ ratios of rocks and inclusions in popping
685 rocks of the mid Atlantic ridge and their bearing on the problem of isotopic composition
686 of deep-seated carbon. Earth and Planetary Science Letters 29, 413-421.
687 Raquin, A., Moreira, M., Guillon, F., 2008. He, Ne and Ar systematics in single vesicles:
688 Mantle isotopic ratios and origin of the air component in basaltic glasses. Earth and
689 Planetary Science Letters 274, 142-150.
690 Roubinet, C., Moreira, M.A., 2018. Atmospheric noble gases in Mid-Ocean Ridge Basalts:
691 Identification of atmospheric contamination processes. Geochimica et Cosmochimica
692 Acta 222, 253-268.
693 Sarda, P., Graham, D.W., 1990. Mid-ocean ridge popping rocks: implications for
694 degassing at ridge crests. Earth and Planetary Science Letters 97, 268-289.
695 Sarda, P., Moreira, M., 2002. Vesiculation and vesicle loss in Mid Oceanic Ridge basalt
696 glasses: He, Ne, Ar elemental fractionation and pressure influence. Geochimica et
697 Cosmochimica Acta 66, 1449-1458.
698 Sarda, P., Moreira, M., Staudacher, T., 1999. Argon-lead isotopic correlation in Mid-
699 Atlantic Ridge Basalts. Science 283, 666-668.
700 Smith, D.K., Escartín, J., Schouten, H., Cann, J.R., 2008. Fault rotation and core complex
701 formation: Significant processes in seafloor formation at slow-spreading mid-ocean
702 ridges (Mid-Atlantic Ridge, 13°–15°N). Geochemistry, Geophysics, Geosystems 9,
703 Q03003.
704 Smye, A.J., Jackson, C.R.M., Konrad-Schmolke, M., Hesse, M.A., Parman, S.W., Shuster, D.L.,
705 Ballentine, C.J., 2017. Noble gases recycled into the mantle through cold subduction
706 zones. Earth and Planetary Science Letters 471, 65-73.

Staudacher, T., Sarda, P., Richardson, S.H., Allègre, C.J., Sagna, I., Dmitriev, L.V., 1989. Noble gases in basalt glasses from a Mid-Atlantic ridge topographic high at 14°N: geodynamic consequences. Earth and Planetary Science Letters 96, 119-133.
Stroncik, N.A., Niedermann, S., 2016. Atmospheric contamination of the primary Ne and Ar signal in mid-ocean ridge basalts and its implications for ocean crust formation. Geochimica et Cosmochimica Acta 172, 306-321.
Trieloff, M., Kunz, J., Clague, D.A., Harrison, D., Allègre, C.J., 2000. The Nature of pristine noble gases in mantle plumes. Science 288, 1036-1038.
Tucker, J.M., Mukhopadhyay, S., Gonnermann, H.M., 2018. Reconstructing mantle carbon and noble gas contents from degassed mid-ocean ridge basalts. Earth and Planetary Science Letters 496, 108-119.
Tucker, J.M., Mukhopadhyay, S., Schilling, J.-G., 2012. The heavy noble gas composition of the depleted MORB mantle (DMM) and its implications for the preservation of heterogeneities in the mantle. Earth and Planetary Science Letters 355-356, 244-254.
Wilson, S.C., Murton, B.J., Taylor, R.N., 2013. Mantle composition controls the development of an Oceanic Core Complex. Geochemistry, Geophysics, Geosystems 14, 979-995.

Table 1. Laser ablation CO_2 and noble gas abundances (in cm^3 STP) for individual pierced vesicles. The ablation duration is indicated in brackets and the symbol ≠ denotes anomalous vesicles (section 3.1). The piece number (#) is detailed in Table S1 and the depth indicates the distance between the sample surface and the vesicle. Vesicle volumes were calculated using the 3D Object Counter plugin of ImageJ. Errors are 1σ uncertainties, n.d. stands for not determined. Longitude, latitude and depth of sample recovery are indicated in brackets (figure 1).

Sample	#	Depth µm	Volume $x10^6$ $µm^3$	Pressure Torr	CO_2 $x10^{-3}$ cm^3	s	^4He $x10^{-7}$ cm^3	s	^{22}Ne $x10^{-13}$ cm^3	s	^{36}Ar $x10^{-12}$ cm^3	s
Sample AL4818-003 (-45.011, 13.774, -3672 m)												
V1 *(2'50")*	1	63	68.6	0.2270	8.21	0.77	2.24	0.10	4.56	0.26	12.5	0.1
V2 *(50")*	1	102	276.6	0.9990	36.1	3.4	9.36	0.40	23.9	0.57	53.3	0.3
V3 *(35")*	1	70	96.9	0.3235	11.7	1.1	3.10	0.13	7.36	0.29	17.3	0.1
V4 *(1'47")*	1	63	105.4	0.3226	11.7	1.1	2.94	0.13	6.33	0.28	16.7	0.1
V5 *(40")*	1	78	77.4	0.2292	8.29	0.78	2.41	0.10	6.40	0.28	13.7	0.1
V6 *(2'10")*	1	157	109.9	0.3103	11.2	1.1	2.97	0.02	6.95	0.46	16.4	0.2
Sample AL4820-036 (-45.010, 13.767, -3718 m)												
V1 *(23")*	1	80	84.0	0.2140	7.74	0.73	1.96	0.02	5.31	0.44	11.0	0.1
V2 *(23")*	1	46	78.6	0.2809	10.2	1.0	2.56	0.03	6.82	0.52	14.4	0.2
V3 *(1'05")*	1	86	267.4	0.9489	34.3	3.2	8.40	0.09	22.0	1.5	48.0	0.6
V4 *(27")*	1	17	47.3	0.1733	6.27	0.59	1.52	0.05	3.48	0.28	8.47	0.21
V5 *(2'10")*	1	108	75.3	0.2550	9.23	0.87	2.29	0.08	5.24	0.30	13.2	0.3
V6 *(2'35")*	1	80	48.8	0.1501	5.43	0.51	1.34	0.05	2.87	0.27	7.56	0.19
V7 *(35")*	1	23	36.5	0.1361	4.92	0.46	1.17	0.04	2.49	0.26	6.82	0.17
V8 *(5'30")*$^{\neq}$	1	8.6	6.1	0.0187	0.68	0.07	0.11	0.01	n.d.	n.d.	1.13	0.05
V9 *(1'35")*	1	112	2896.8	2.6227	94.9	8.9	21.8	0.07	54.9	1.8	127	3
Sample AL4820-041 (-45.002, 13.770, -3645 m)												
V1 *(1'18")*	2	60	422.3	1.0920	39.5	3.7	10.5	0.1	26.1	1.1	31.5	0.2
V2 *(4'39")*	2	17	12.6	0.0437	1.58	0.15	0.47	0.01	0.98	0.25	1.22	0.04
V3 *(5'12")*	1	87	133.8	0.4420	16.0	1.5	4.68	0.03	10.6	0.51	12.5	0.1
V4 *(4'47")*$^{\neq}$	3	127	539.2	0.0284	1.03	0.10	0.005	0.008	0.38	0.24	0.96	0.04
Sample AL4820-055 (-45.010, 13.773, -3665 m)												
V1 *(5'45")*	1	94	42.0	0.1375	4.97	0.47	1.45	0.01	3.78	0.33	7.85	0.09
V2 *(1'25")*$^{\neq}$	1	37	316.1	1.0827	39.2	3.7	8.43	0.04	24.6	1.4	56.5	0.6
V3 *(2'16")*	1	102	361.2	1.2069	43.7	4.1	11.3	0.3	26.6	1.4	62.4	0.6
V4 *(4'57")*	1	78	259.7	0.9467	34.3	3.2	9.47	0.28	21.6	1.2	47.8	0.5
V5 *(2'48")*$^{\neq}$	1	31	47.8	0.0253	0.92	0.09	0.04	0.01	10.2	0.5	44.7	0.4
Sample AL4820-058 (-45.009, 13.774, -3684 m)												
V1 *(2'15")*	1	22	30.5	0.0932	3.37	0.32	0.92	0.03	2.22	0.26	5.10	0.57
V2 *(37")*$^{\neq}$	1	17	89.8	0.2932	10.6	1.0	0.05	0.01	5.72	0.33	17.0	0.2
V3 *(2'08")*	1	29	95.5	0.3102	11.2	1.1	3.01	0.09	6.80	0.35	16.2	0.1
V4 *(2'43")*	1	28	43.1	0.1613	5.84	0.55	1.56	0.05	3.60	0.28	8.45	0.08
V5 *(4'20")*	1	29	28.9	0.0812	2.94	0.28	0.78	0.03	1.62	0.25	4.28	0.05
Sample 2πD43												
V1 *(4'42")*	1	24	525.9	1.6844	60.9	5.7	15.2	0.56	40.1	2.0	46.0	1.3
V2 *(3')*$^{\neq}$	1	61	436.2	0.0130	0.47	0.05	0.01	0.01	5,930	397	13,221	167
V3 *(30")*	1	66	58.3	0.2355	8.52	0.80	2.24	0.03	5.28	0.44	6.18	0.09
V4 *(1'01")*	1	72	74.4	0.2327	8.42	0.79	2.50	0.03	5.02	0.42	7.03	0.10

Table 2. Vesicle elemental and isotopic ratios obtained by laser ablation. The symbol ≠ denotes anomalous vesicles (section 3.1). $^{3}He/^{4}He$ ratio is presented relative to atmosphere (Ra), where 1 Ra is equal to 1.384×10^{-6} (Clarke et al., 1976). $^{40}Ar^{*}$ is radiogenic ^{40}Ar. We use the value of 295.5 for the atmospheric $^{40}Ar/^{36}Ar$ ratio. Errors are 1σ uncertainties, n.d. stands for not determined.

Sample	$CO_2/^{3}He$	s	$^{3}He/^{4}He$	s	$^{20}Ne/^{22}Ne$	s	$^{21}Ne/^{22}Ne$	s	$^{38}Ar/^{36}Ar$	s	$^{40}Ar/^{36}Ar$	s	$^{4}He/^{40}Ar^{*}$	s
	$x10^{9}$		(xRa)											
Sample AL4818-003														
V1	3.19	0.34	8.29	0.21	12.25	0.15	0.0621	0.0020	0.1879	0.0006	16040	247	1.13	0.05
V2	3.36	0.36	8.30	0.21	11.85	0.05	0.0539	0.0011	0.1893	0.0008	15275	80	1.17	0.05
V3	3.26	0.35	8.36	0.21	11.81	0.08	0.0541	0.0016	0.1861	0.0005	16052	171	1.14	0.05
V4	3.38	0.36	8.48	0.22	12.19	0.09	0.0566	0.0018	0.1862	0.0005	16342	179	1.10	0.05
V5	2.98	0.32	8.35	0.21	12.04	0.08	0.0535	0.0024	0.1876	0.0006	16303	210	1.10	0.05
V6	3.36	0.32	8.11	0.11	12.05	0.09	0.0566	0.0013	0.1882	0.0006	16256	199	1.14	0.02
Sample AL4820-036														
V1	3.46	0.34	8.28	0.20	12.08	0.14	0.0565	0.0017	0.1892	0.0010	15707	439	1.15	0.04
V2	3.53	0.35	8.13	0.20	11.96	0.10	0.0555	0.0013	0.1900	0.0009	16251	349	1.11	0.03
V3	3.58	0.35	8.24	0.21	12.10	0.06	0.0572	0.0010	0.1906	0.0009	15851	147	1.12	0.02
V4	3.51	0.38	8.50	0.37	12.50	0.16	0.0572	0.0022	0.1869	0.0015	16267	545	1.12	0.06
V5	3.44	0.38	8.48	0.37	12.44	0.12	0.0602	0.0020	0.1903	0.0014	16229	362	1.08	0.05
V6	3.45	0.38	8.51	0.38	12.76	0.25	0.0586	0.0030	0.1867	0.0014	16109	601	1.12	0.06
V7	3.51	0.38	8.69	0.38	12.28	0.24	0.0606	0.0033	0.1891	0.0015	15940	638	1.09	0.06
V8≠	4.64	0.64	10.00	0.48	n.d.	n.d.	n.d.	n.d.	0.1910	0.0041	13327	3132	0.71	0.18
V9	3.64	0.40	8.63	0.38	12.14	0.04	0.0583	0.0009	0.1884	0.0014	16145	133	1.08	0.05
Sample AL4820-041														
V1	3.26	0.31	8.36	0.10	12.31	0.07	0.0573	0.0010	0.1880	0.0008	25173	336	1.34	0.02
V2	2.89	0.28	8.48	0.16	13.38	0.43	0.0632	0.0050	0.1786	0.0035	26470	4928	1.45	0.28
V3	2.88	0.27	8.58	0.11	12.44	0.07	0.0591	0.0016	0.1915	0.0006	27073	509	1.40	0.03
V4≠	4932	21599	0.33	1.32	11.70	0.51	0.0518	0.0074	0.2006	0.0040	26089	6300	0.02	0.03
Sample AL4821-055														
V1	3.05	0.29	8.17	0.12	12.13	0.17	0.0574	0.0023	0.1886	0.0007	16149	373	1.16	0.03
V2≠	3.77	0.36	8.91	0.12	12.22	0.06	0.0585	0.0008	0.1885	0.0007	16311	88	0.93	0.01
V3	3.33	0.34	8.38	0.21	12.07	0.06	0.0578	0.0007	0.1882	0.0007	16089	84	1.15	0.04
V4	3.16	0.32	8.28	0.20	12.15	0.06	0.0573	0.0010	0.1884	0.0009	15915	90	1.27	0.04
V5≠	18.0	4.4	9.33	0.56	9.71	0.08	0.0296	0.0011	0.1884	0.0004	2418	14	0.04	0.01
Sample AL4821-058														
V1	3.28	0.34	8.11	0.21	11.85	0.16	0.0471	0.0027	0.1872	0.0010	15721	551	1.16	0.06
V2≠	274	56	5.60	0.37	11.83	0.11	0.0547	0.0015	0.1886	0.0006	16146	179	0.02	0.00
V3	3.31	0.34	8.14	0.20	12.02	0.11	0.0576	0.0010	0.1894	0.0006	16261	189	1.17	0.04
V4	3.26	0.33	8.25	0.22	11.86	0.15	0.0568	0.0018	0.1893	0.0007	16220	351	1.16	0.05
V5	3.31	0.36	8.25	0.27	12.65	0.34	0.0565	0.0036	0.1881	0.0011	16446	757	1.13	0.07
Sample 2πD43														
V1	3.36	0.35	8.61	0.17	12.47	0.10	0.0596	0.0019	0.1916	0.0011	25866	330	1.29	0.06
V2≠	287	241	0.98	0.49	9.67	0.04	0.0289	0.0004	0.1882	0.0008	299	2	0.03	0.02
V3	3.23	0.32	8.51	0.21	12.53	0.16	0.0586	0.0016	0.1880	0.0011	26809	1443	1.37	0.08
V4*	2.92	0.29	8.32	0.21	(13.12*)	0.16	(0.0661*)	0.0024	0.1889	0.0012	26191	1243	1.38	0.07

*CO_2 interference is overcorrected. This bubble was targeted just after vesicle V3 of sample 2πD43 and strong CO_2 memory effects were observed when analyzing neon from vesicle V4.

Table 3. Noble gas abundances and isotopic compositions obtained by crushing in vacuum. $^{3}He/^{4}He$ ratio is presented relative to atmosphere (Ra), where 1 Ra is equal to $1.384x10^{-6}$ (Clarke et al., 1976). $^{40}Ar^{*}$ is radiogenic ^{40}Ar. We use the value of 295.5 for the atmospheric $^{40}Ar/^{36}Ar$ ratio. Errors are 1σ uncertainties, n.d. stands for not determined. The weights of samples 055 and 058 are less accurate because they were determined inside the glove box. The Cl/K and H_2O/Ce ratios are from Jones et al. (2019).

Figure 1. Bathymetric map showing the location of the samples from cruise AT33-03 of *R/V Atlantis* on the Mid-Atlantic Ridge analyzed in this contribution. The extinct oceanic core complex (Smith et al., 2008) is visible in the east of the left image. The popping rock 2πD43 was recovered by dredging close to 13°46'N (Bougault et al., 1988). The image on the right is a zoom of the white rectangle.

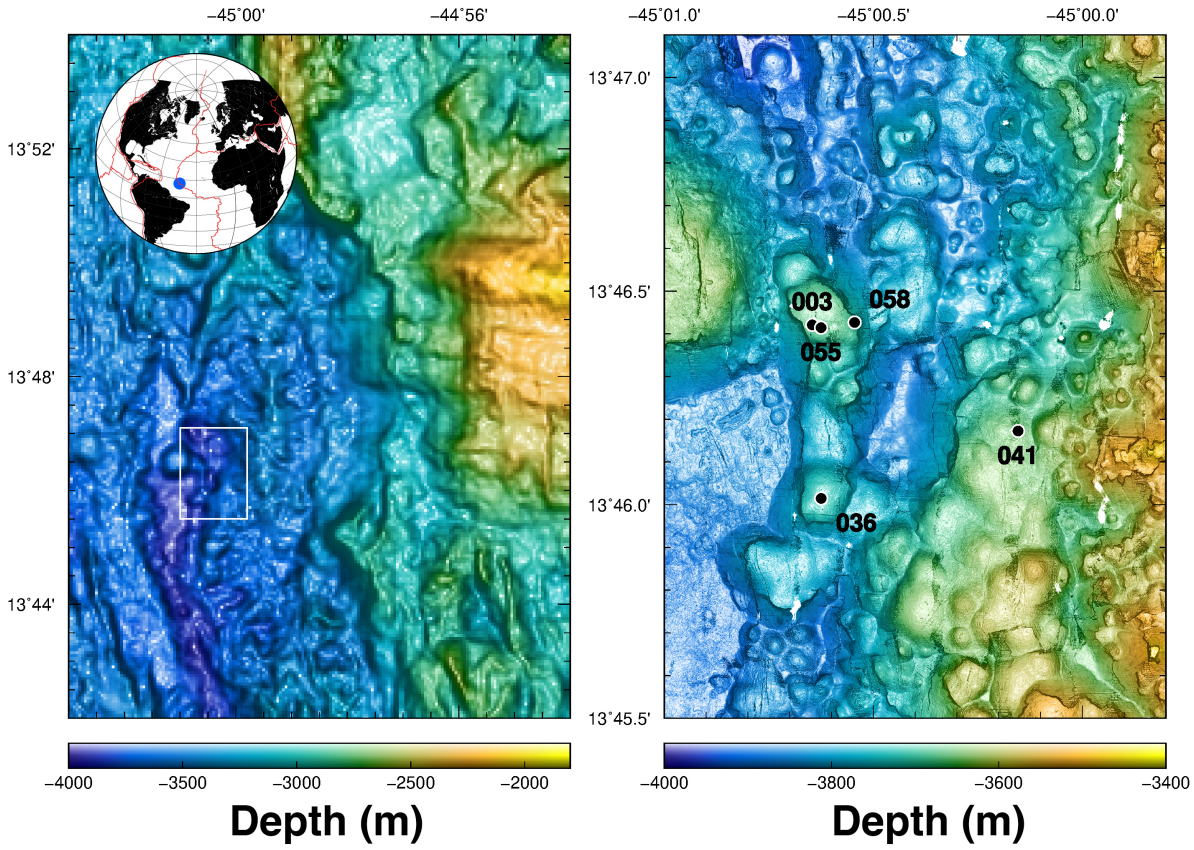

Figure 2. Neon-neon isotope diagram comparing (a) step-crushing data and (b) laser ablation data. Data from Moreira et al. (1998) for the popping rock 2πD43 are indicated with the grey squares. The black star indicates the mantle composition from the popping rock 2πD43, the mauve star corresponds to the mean vesicle composition (vesicles with $^{20}Ne/^{22}Ne > 12$). ASW, *air-saturated seawater*. Strong CO_2 memory effects were observed during analysis of vesicle V4-2πD43. Vesicle V2-041 is one of the smallest vesicles analyzed. The neon compositions of these vesicles are thus unreliable. *MORB line* as defined by the 2πD43 data of Moreira et al. (1998).

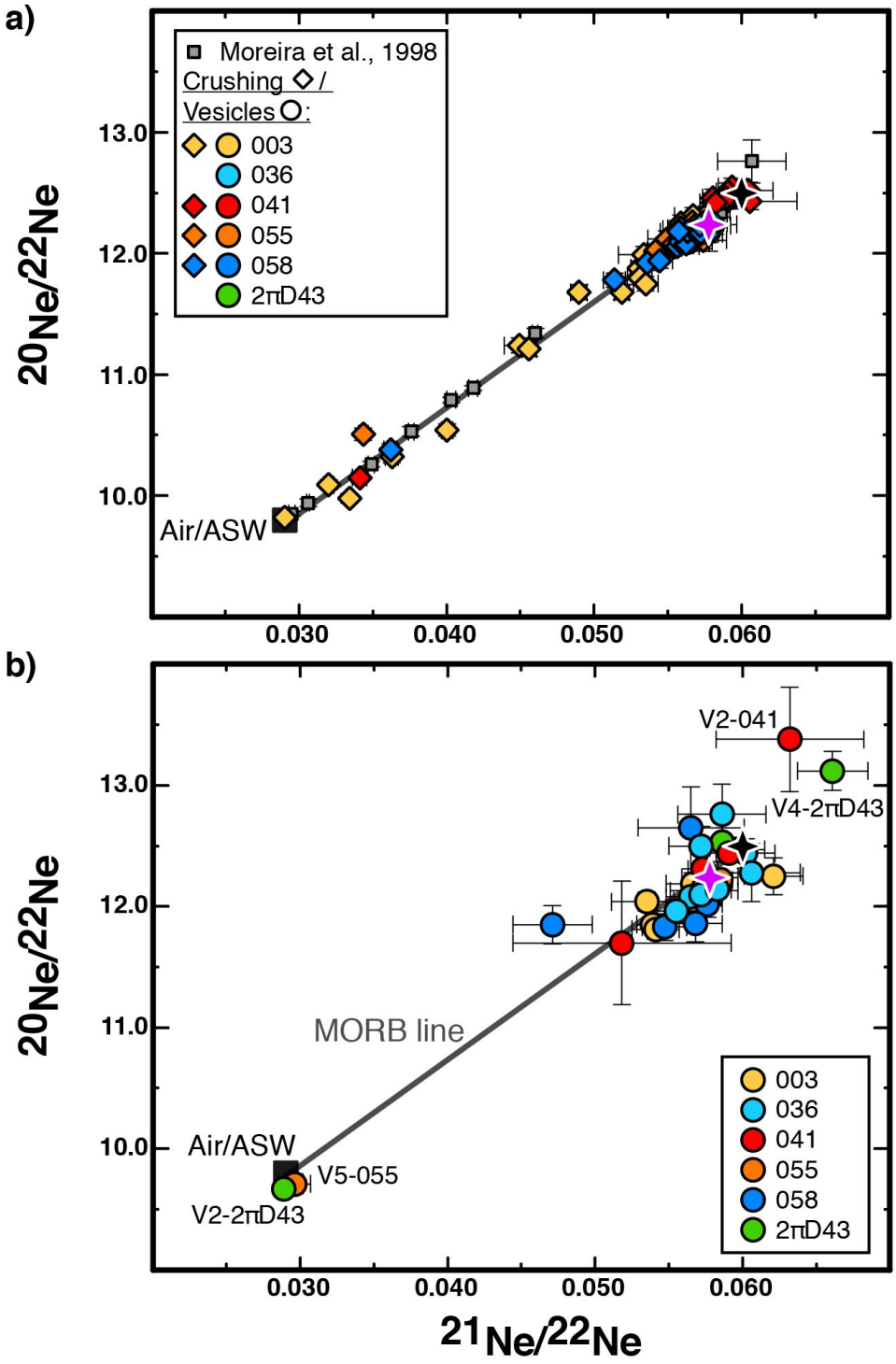

Figure 3. $^{40}Ar/^{36}Ar$ ratios vs. $^{20}Ne/^{22}Ne$ ratios for the step-crushing and laser ablation data. Data from Moreira et al. (1998) for the popping rock 2πD43 are indicated with the grey squares. The black star indicates the mantle composition from the popping rock 2πD43, the mauve star corresponds to the mean vesicle composition (vesicles with $^{20}Ne/^{22}Ne > 12$). ASW, *air-saturated seawater*. The curvatures r of the hyperbolas are defined by the ratio $(^{36}Ar/^{22}Ne)_{air/SW} / (^{36}Ar/^{22}Ne)_{mantle}$. The neon compositions of V2-041 and V4-2πD43 are unreliable (section 3.3).

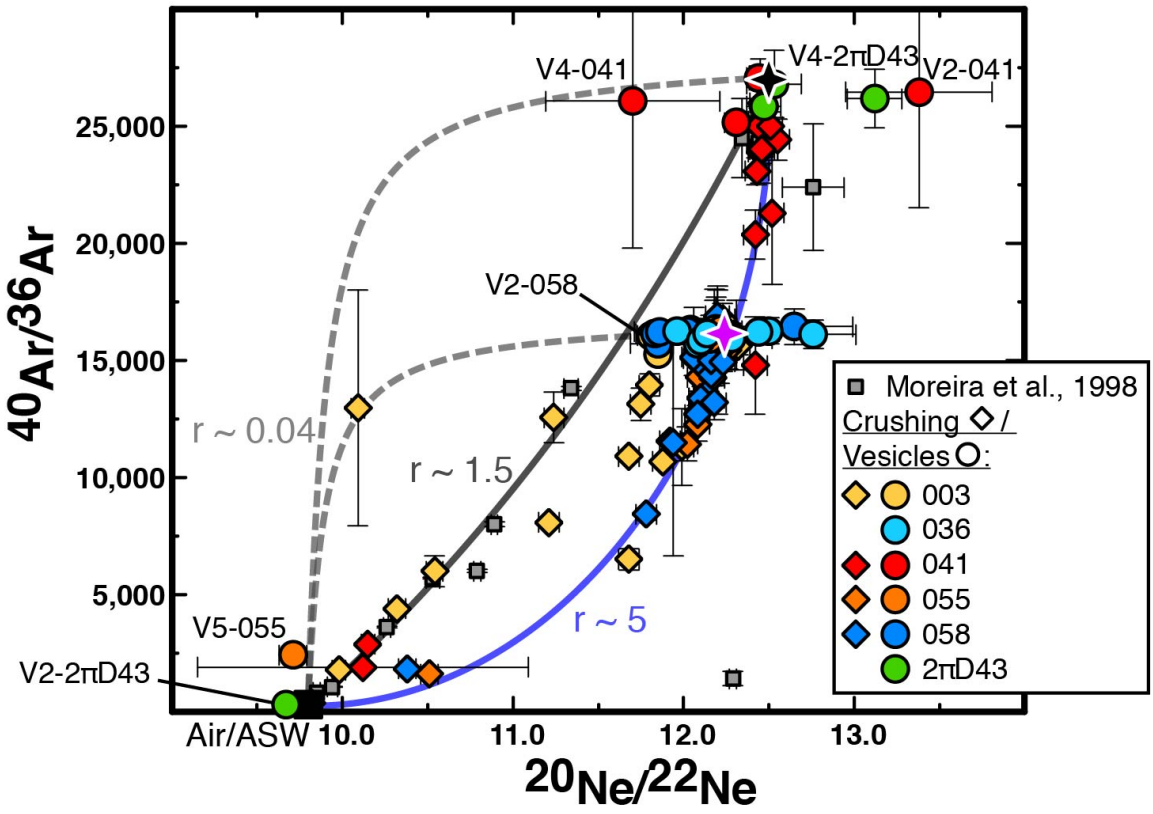

Figure 4. $^{20}Ne/^{22}Ne$ ratios vs. $^{3}He/^{22}Ne$ ratios for the step-crushing and laser ablation data. Data from Moreira et al. (1998) for the popping rock 2πD43 are indicated with the grey squares. The black star indicates the mantle composition from the popping rock 2πD43 (Moreira et al., 1998). ASW, *air-saturated seawater*.

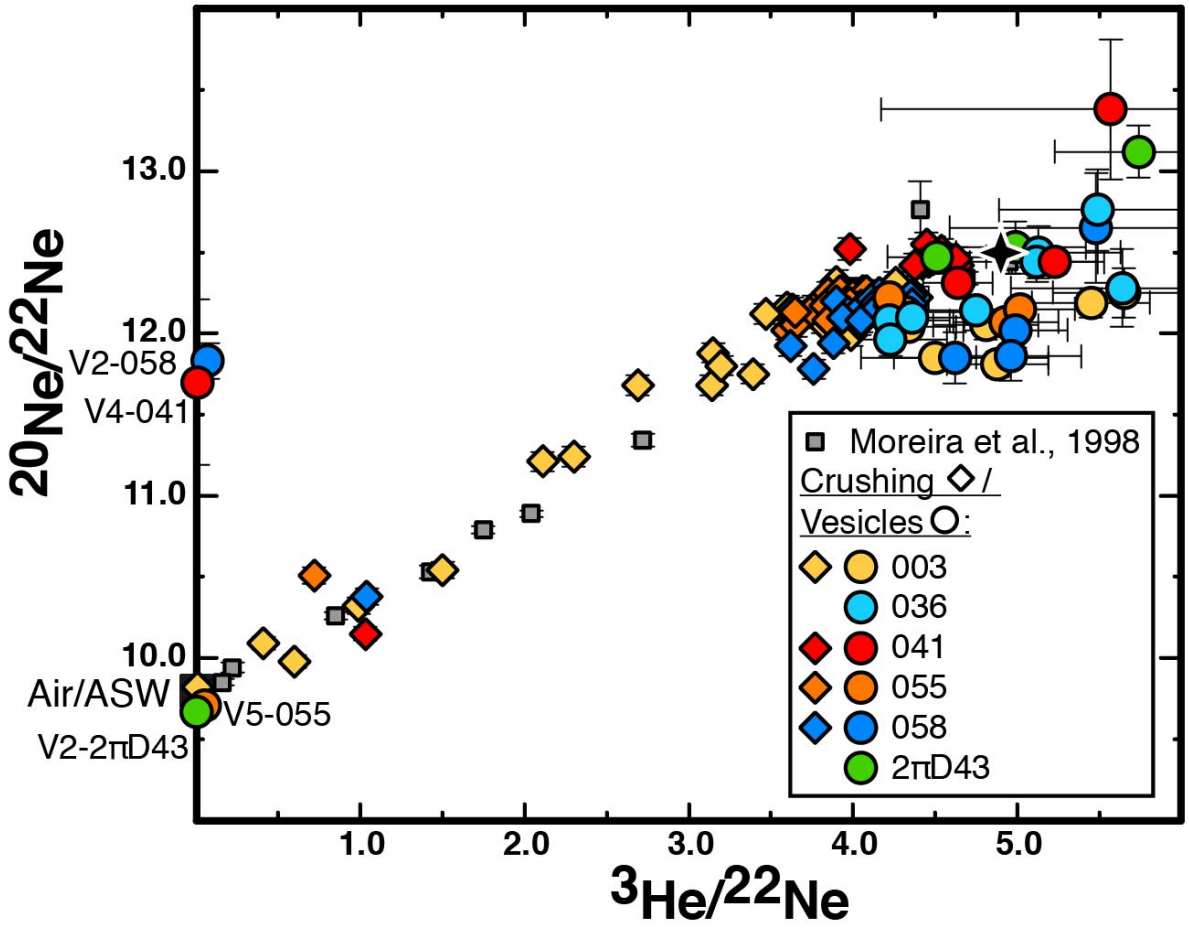

Figure 5. $^{20}Ne/^{22}Ne$ ratio vs. $^{36}Ar/^{22}Ne$ ratio for the step-crushing and laser ablation data (a). The bottom panel (b) shows only the vesicles. Data from Moreira et al. (1998) for the popping rock 2πD43 are indicated with the grey squares. Air (black square), air-saturated seawater at 25 °C (light blue square), air-saturated seawater at 0 °C (dark blue square), air-saturated seawater data are from Ozima and Podosek (2002). The black star indicates the mantle composition from the popping rock 2πD43, the mauve star corresponds to the mean vesicle composition (vesicles with $^{20}Ne/^{22}Ne > 12$). The crushing data with $^{36}Ar/^{22}Ne > 30$ and $^{20}Ne/^{22}Ne > 12$ correspond to analyses with low ^{36}Ar contents and so these $^{36}Ar/^{22}Ne$ ratios may be poorly constrained.

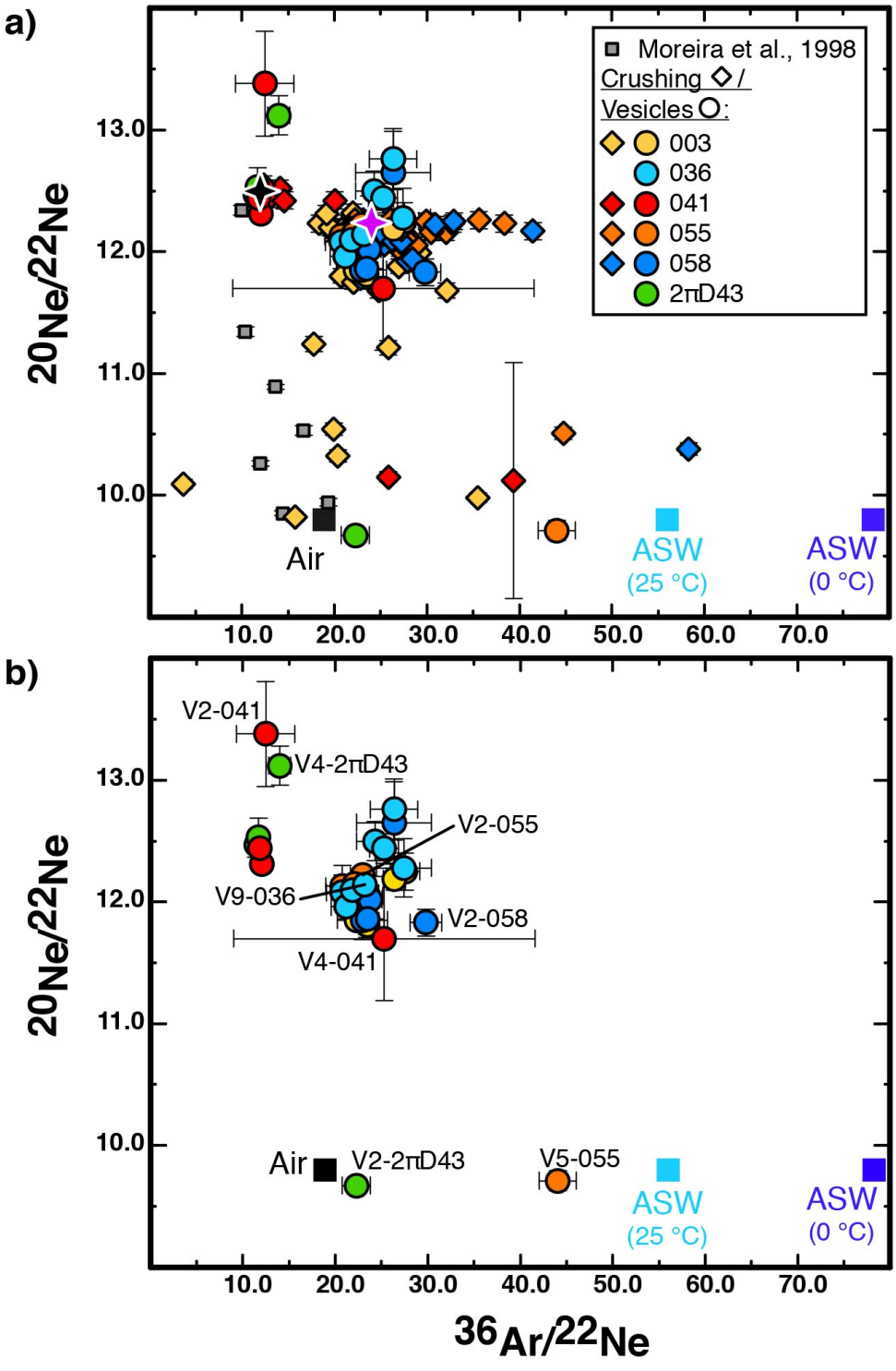

Figure 6. ^{36}Ar contents (in cm^3 STP) of the vesicles associated with their volumes. Samples 041 and 2πD43 plot on a different line than samples 003, 036, 055 and 058. The linear regression coefficients are indicated for the two lines. Vesicles V5 055 and V2 2πD43 are strongly contaminated, vesicle V4 041 has lost gases and vesicle V9 036 is special due to coalescence (section 3.1) and so they are not represented.